Earth Planet. Sci. Lett. 646 (2024) 118984

Contents lists available at ScienceDirect

Earth and Planetary Science Letters

journal homepage: www.elsevier.com/locate/epsl

Rheological arrest vs. rapid growth of bubbles in crystal-rich magma

P. Moitra

Department of Geosciences, University of Arizona, Tucson, AZ 85721, USA

ARTICLE INFO

Editor: C.M. Petrone

Dataset link: https://doi.org/10.25422/azu.data.26359957

Keywords:
Extensional rheology
Shear rheology
Effusive-explosive eruptions
Bubble growth
Conduit flow model
Yield stress-limited growth

ABSTRACT

Effusive to violently explosive eruptions of crystal-rich magmas are frequently found in volcanic records. The competing effects of rheological stiffening of magma in the presence of crystals and magma overpressure build-up in the presence of bubbles typically control the volcanic explosivity. The bubble growth exerts extensional stress on its wall, i.e., the melt+crystal matrix surrounding it. However, the rheology of crystal-rich magma under such extension along with the effect of crystals on bubble growth, are poorly understood. From analog experiments, this study finds that crystalline magma exhibits yield stress and power-law rheology with broadly comparable values under extensional and shear deformation. The pressure loss due to the presence of yield stress can significantly affect bubble growth in magma. Using bubble growth model in crystallizing magma, this study shows that the yield stress in melt+crystal matrix surrounding bubbles can exceed gas overpressure, preventing bubble growth. The model parameter search exhibits three regimes of bubble growth in crystallizing magmas for a wide range of magma decompression and crystallization rates during effusive to explosive volcanic eruptions. In the yield stress-limited regime, a complete halt in bubble growth can occur at a relatively small viscosity of crystal-rich basaltic magma (~10^6 Pa s), and depending on the crystalline system, at a crystal volume as low as ~30%. On the other hand, at relatively higher magma decompression rates, significant magma expansion associated with relatively rapid bubble growth, even at a relatively high normalized crystal content of >90%, could cause magma fragmentation and eruption explosivity. This study demonstrates that small changes in eruption conditions, such as magma decompression rates and crystallization rates, can cause significant changes in bubble growth dynamics with implications for transitions in volcanic eruption styles.

1. Introduction

The exsolution of dissolved volatiles into bubbles and their growth dynamics drive magma fragmentation and the styles of volcanic eruptions (e.g., Sparks, 1978; Proussevitch et al., 1993; Toramaru, 1995; Zhang, 1999; Papale, 1999; Lensky et al., 2004; Gonnermann and Manga, 2007; Ichihara, 2008; Namiki and Manga, 2008; Oppenheimer et al., 2015; Suckale et al., 2016; Gardner et al., 2023). Magmas in effusive to violently explosive volcanic eruptions often contain abundant crystals (e.g., Melnik and Sparks, 1999; Sable et al., 2006; Lavallée et al., 2007; Sable et al., 2009; Okumura et al., 2016; Arzilli et al., 2019; Andrews and Befus, 2020; Petrone et al., 2022). While rheological stiffening of magma in the presence of abundant crystals (e.g., Mader et al., 2013) promotes outgassing, plug formation, and eruption periodicity (e.g., Hammer et al., 1999; Melnik and Sparks, 1999; Gurioli et al., 2014), it may also cause high eruption explosivity (e.g., Moitra et al., 2013, 2018; Arzilli et al., 2019; Okumura et al., 2019; La Spina et al., 2021; Bamber et al., 2022, 2024). Thus, understanding the effect of the non-Newtonian rheology of crystalline magma on bubble growth could provide better insights into the effusive-explosive transitions in volcanic eruption styles.

A growing bubble in ascending and crystallizing magma exerts an extensional stress on the wall (melt+crystal matrix) surrounding it. This plays a key role in driving magma expansion and fragmentation (e.g., Zhang, 1999; Villermaux, 2012; Moitra et al., 2013; Jones et al., 2019; Okumura et al., 2019). Thus, the characterization of the rheological properties of crystal-rich magma under extensional deformation is important but currently lacking, as compared to its rheology under shear (e.g., Caricchi et al., 2007; Cimarelli et al., 2011; Mueller et al., 2011; Avard and Whittington, 2012; Lev et al., 2012; Picard et al., 2013; Vona et al., 2013; Faroughi and Huber, 2015; Moitra and Gonnermann, 2015; Soldati et al., 2016; Bergantz et al., 2017; Kolzenburg et al., 2022). It is important to characterize the rheological properties under extensional deformation, especially in crystal-rich systems, where crystal-crystal interactions could significantly affect the magma rheology, and therefore, bubble growth.

E-mail address: pmoitra@arizona.edu.

https://doi.org/10.1016/j.epsl.2024.118984
Received 8 April 2024; Received in revised form 24 July 2024; Accepted 31 August 2024

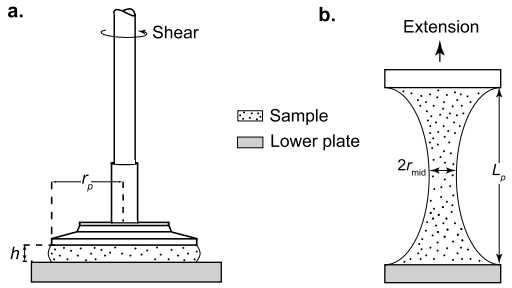

Fig. 1. Schematic diagrams (not to scale) show the (**a**) shear and (**b**) extensional experimental set-ups. The symbol definitions are given under 'Notation'.

The viscosity of crystallizing magma increases exponentially with increasing crystal content until the development of crystal-crystal interaction or a yield stress, i.e., the minimum stress required for the mobility of crystalline magma. Recent advances in our understanding of magma rheology in the presence of crystals show the existence of such yield stress, often referred to as an apparent yield stress (Barnes, 1999), that is developed due to crystal jamming when a critical crystal volume fraction is reached (e.g., Ryerson et al., 1988; Pinkerton and Stevenson, 1992; Hoover et al., 2001; Walsh and Saar, 2008; Cimarelli et al., 2011; Mueller et al., 2011; Mader et al., 2013; Moitra and Gonnermann, 2015). For practical purposes, the effect of this apparent yield stress is usually neglected in characterizing the dynamics of crystal-rich magma during eruptions, and therefore, has remained poorly understood.

Since bubble growth causes an extensional deformation to the surrounding melt+crystal matrix while the bulk flow of magma experiences a shear deformation along the conduit wall, it is important to evaluate the yet-to-be-determined relationships between the rheological properties of crystalline magma under shear and extensional deformation. Therefore, using analog laboratory experiments, this study first characterizes the rheological properties of crystal-rich magma under extension and compare them with the outcomes under shear deformation. Then, using the experimental outcomes in a model of bubble growth in crystallizing magma, it investigates the effects of crystals on the bubble growth dynamics during volcanic eruptions. The implications of the experimental and numerical findings on the effusive-explosive styles of volcanic eruptions are discussed.

2. Rheology experiments

2.1. Analog suspension

Experiments using dense particulate suspension analogous to silicate melt suspended with abundant crystals are performed to characterize crystal-rich magma rheology under shear and extensional deformation (Fig. 1). The suspension was made with solid glass spheres with ~ 3-10 μm diameter (inset of Fig. 2a) and ~2500 kg m^{-3} density, suspended in a Newtonian silicone liquid (970 kg m^{-3} density), i.e., the viscosity of the liquid (~111 Pa s) does not change under the applied stresses and strain rates in the experiments.

The glass spheres and the liquid were mixed at a particle volume fraction of ~0.55, which is close to the maximum packing of such a particulate system (Moitra and Gonnermann, 2015). The liquid and particles were mixed and deaerated using a planetary mixer. The suspension characteristics and the dynamic similarity are discussed in section 3.1.1. The rheology experiments were performed using new samples for each experiment, and under a range of stress and strain rates at ambient temperature.

2.2. Shear rheology

For shear experiments, the liquid+particle suspension was placed in a parallel plate set-up (Fig. 1a) in a rotational rheometer. The gap between the parallel plate or sample thickness was 1 mm for all experiments. The suspension was deformed under continuously varying shear stress (up to 6000 Pa), where the lower plate was stationary and the upper plate was rotating under the applied torque, M. To avoid wall slip, sand-blasted upper and lower plates were used in the experiments.

For a given applied torque and the resultant angular velocity (Ω) of the upper plate, the shear stress, τ_S, is calculated using (Mezger, 2006):

$$\tau_S = \frac{2M}{\pi r_p^3}, \tag{1}$$

where the shear rate, $\dot{\gamma}_S$, is calculated using:

$$\dot{\gamma}_S = \frac{\Omega r_p}{h}. \tag{2}$$

Here h is the sample thickness and r_p is the upper plate radius (~12.5 mm). A small oscillatory shear was applied at the beginning of each experiment to avoid any artifacts due to sample placement (Moitra and Gonnermann, 2015).

2.3. Extensional rheology

To characterize extensional rheology, the dense particulate suspension was placed between two parallel plates (Fig. 1b) in a tensile tester. To achieve a purely uniaxial extension and to avoid any effects of shear deformation, the top plate was moved upward at a constant stretch rate with an exponential velocity profile (e.g., McKinley and Sridhar, 2002), such that

$$L_p(t) = L_0 \exp(\dot{E}t), \tag{3}$$

where L_p is the plate separation length as a function of time, with a starting length of L_0. $\dot{E}$ is the axial stretch rate, and t is the time.

A small strain was applied prior to each experiment to avoid any artifacts due to the placement of the sample (White et al., 2010). Ignoring negligible effect of inertia, the extensional stress, τ_E, is defined as (Szabo, 1997):

$$\tau_E = \frac{F}{\pi r_{mid}^2} + \frac{1}{2}\frac{\rho g(\pi L_0 {r_0}^2)}{\pi r_{mid}^2} - \frac{\sigma}{r_{mid}}. \tag{4}$$

Here F is the tensile force, r_{mid} is the mid-radius of the sample, ρ is the density of the suspension, σ is the surface tension, g is the gravitational acceleration, and r_0 is the initial mid-radii of the sample.

The extensional rate of deformation, $\dot{\gamma}_E$, is given by

$$\dot{\gamma}_E(t) = \frac{-2}{r_{mid}}\frac{dr_{mid}}{dt}, \tag{5}$$

where the Hencky strain, $\gamma_E = 2ln(r_0/r_{mid})$, was ≈1-2.5 (see Supplementary Material). To avoid any effect of shear at the edges, the ratio between the initial length and the initial radius of the sample for all experiments was ≥ 1 (e.g., McKinley and Sridhar, 2002, see supplementary material). Each experiment was recorded, and the images were used to measure the change in the mid-radius of the sample from conservation of fluid volume and with the aid of photographs of the extending cylindrical filament. The axial stretch rate was varied between 0.05-2 s^{-1}, which is larger than the capillary drainage timescale of the suspension. For experiments at high strain rates, the samples experienced ductile to brittle-like fracturing (Moitra et al., 2018), and therefore, the stress-strain rate relationship prior to sample failure is evaluated.

3. Results and discussion

3.1. Rheological characterization of dense suspension

The experimental stress-strain rate data from shear and extensional rheology experiments exhibit that the rate of deformation decreases with decreasing stress (Fig. 2). The stress-strain rate data approximately

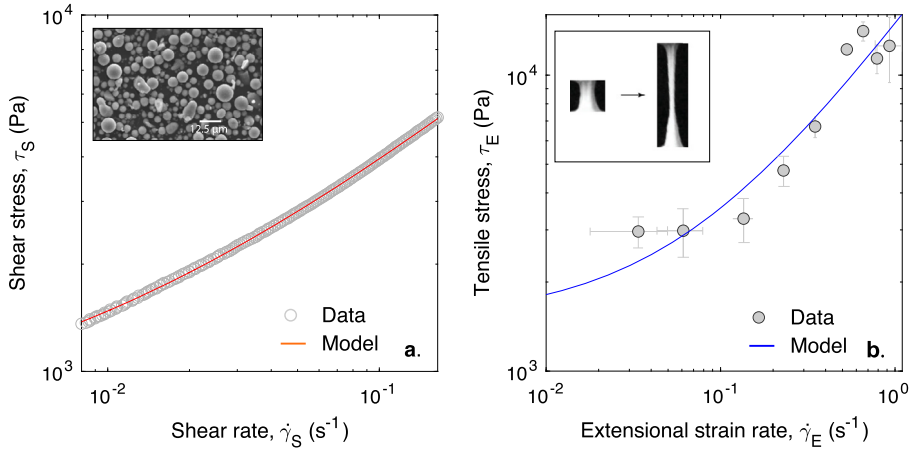

Fig. 2. Stress as a function of the rate of deformation under shear (**a**) and extensional (**b**) deformation. The experimental data were fitted by Equation (6) (solid lines). The inset in **a** shows the backscattered electron image of the analog spherical glass beads. The error in **a** is smaller than the symbol size. The error bars in **b** correspond to repeat experiments and errors associated with estimates of sample mid-radii from experimental images. The inset in **b** shows snapshots of the extensional experiment at 0.05 s^{-1} stretch rate with an initial sample mid-radius (r_{mid}) of 4 mm, where the sample was stretched until r_{mid}~1 mm.

plateaus at lower rates of deformation. This indicates the presence of yield stress, i.e., the particulate suspension is not likely to deform at an applied stress lower than the yield stress.

Accordingly, the stress-strain rate data from both sets of experiments are fitted with the Herschel-Bulkley model (Herschel and Bulkley, 1926) that accounts for both yield stress and power-law rheology:

$$\tau = \tau_y + K\dot{\gamma}^n. \tag{6}$$

Here τ and $\dot{\gamma}$ are the stress and strain rates. τ_y is the yield stress, K is the consistency, and n is the flow index. The data was fitted by minimizing the objective function, O_F, defined as

$$O_F = \sqrt{\frac{1}{N}\sum\left\{\log_{10}(\tau_{\text{measured}}) - \log_{10}(\tau_{\text{predicted}})\right\}^2}, \tag{7}$$

where N is the number of measured data points. τ_{measured} and $\tau_{\text{predicted}}$ are the measured and the predicted stresses, respectively.

Fig. 2 shows that the Herschel-Bulkley model reasonably well-characterizes the non-Newtonian properties of the particulate suspension under shear (O_F = 0.003) and extensional (O_F = 0.077) deformation. τ_y and n obtained from shear and extensional experiments are 703 and 1500 Pa, and 0.62 and 0.82, respectively. K ~1.3×10^4 Pa s^n for both shear and extensional tests. Although the extensional viscosity of a Newtonian fluid is a factor of 3 larger than the zero-shear viscosity, based on the Trouton ratio, this factor may vary for non-Newtonian fluids (e.g., Bird et al., 2015; Dai and Tanner, 2017). The extensional viscosity of the particulate suspension at comparable low strain rates (≈10^{-2} s^{-1}) is similar to that obtained from shear experiments. Future experiments at smaller strain rates (≪10^{-2} s^{-1}), will likely provide further insights into the transient rheology of analog suspensions under extension.

While this study investigates dense suspensions, the rheological properties under extension are expected to depend on the particle volume fraction (e.g., Dai and Tanner, 2017), similar to the case under shear deformation. Thus, for a range of crystal shape and size modality, τ_y can be estimated using the formulations of Moitra and Gonnermann (2015):

$$\tau_y = \tau^*\left[\left(1-\frac{\phi_x}{\phi_m}\right)^{-2} - \left(1-\frac{\phi_c}{\phi_m}\right)^{-2}\right]. \tag{8}$$

Here ϕ_x is the crystal volume fraction and ϕ_m is the maximum packing of the given crystalline system. ϕ_c is the critical fraction of crystals where yield stress develops. The minimum normalized volume fraction for the development of yield stress, $\phi_c/\phi_m \approx 0.15$. For subspherical to high aspect ratio uni- to bi-modal crystalline systems, the fitting parameter, τ^*, varies between 0.20-4.40 (Moitra and Gonnermann, 2015). The estimates of τ_y using τ^* ~1.00 match reasonably well with the values obtained from the experiments in this study (Fig. 3a). Further extensional tests with less dense suspensions would be required to validate the range of values of τ^*.

3.1.1. Dynamic similarity

Using the density and average particle diameter of the analog glass beads, and the viscosity and density of the suspending silicone oil (section 2.1), both the particle Reynolds number (Re_p) and Stokes number (St) are ≪ 1, suggesting that the inertial forces were negligible in our experiments whereas the particles were coupled with the flow. Also, the Peclet (Pe) number >10^3, indicates that the Brownian forces were negligible in the experiments. Using the initial mid-diameter of the sample of ~5 mm, the Ohnesorge (Oh) number is ≫1 in the tensile experiments, indicating a negligible effect of capillary and inertial forces. Furthermore, the settling time scales of the particles in the liquid are on the order of months, which is significantly larger as compared to the experimental time scales (<1 hour), and therefore, particle sedimentation during any experiments was negligible.

In magmatic settings, for millimeter scale (and smaller) crystals suspended in silicate melts with a range of compositions with >2400 kg m^{-3} density, ≥10 Pa s and ≥10^4 Pa s viscosity of silicate melts and crystalline magma, respectively, and ≳10 μm thick melt+crystal matrix surrounding the expanding bubbles, Pe>10^3, St≪1, Re_p≪1 and Oh≫1. Also, because of a small difference in density between crystals and the ascending magma, the settling of crystals in viscous magma is negligible. These suggest that a similarity between the experimental and the natural settings is reasonably justified, and that the experimental outcomes can likely be used to understand the eruption dynamics of magma with a range of compositions.

3.2. Bubble growth in magma with Herschel-Bulkley rheology

Based on the experimental findings, a Herschel-Bulkley type model can be used to estimate bubble growth in crystallizing magma during volcanic eruptions, which is investigated in the next sections.

3.2.1. Bubble growth rate

The effect of Herschel-Bulkley type rheology on bubble growth can be obtained from evaluating the growth rate of bubble in crystal-free magma first. In the absence of body force, in silicate melt with constant density, during bubble growth, the equation of continuity in spherical coordinates is given by (Bird et al., 2015, and references therein)

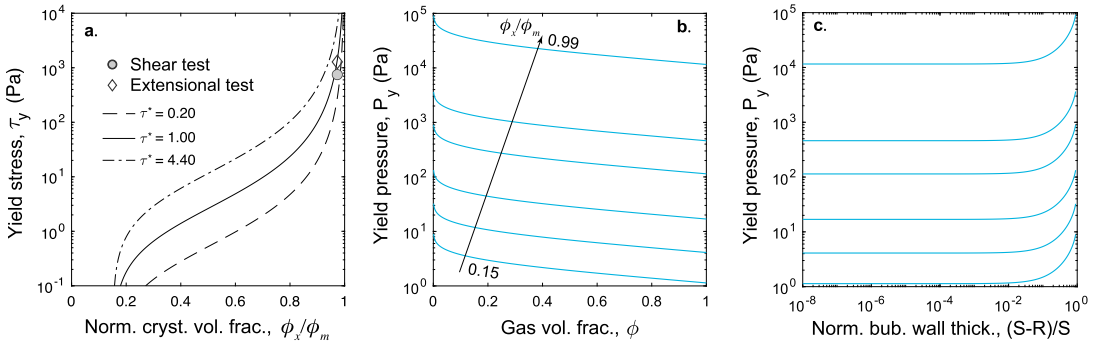

Fig. 3. (**a**) Yield stress, τ_y, as a function of normalized crystal fraction, ϕ_x/ϕ_m. The solid and dashed curves are based on Equation (8). Using $\tau^* = 1$ that reasonably matches with the empirically obtained yield stress values, the pressure reduction (referred to as the yield pressure), P_y, is calculated (Equation (15)) as a function of gas volume fraction, ϕ (**b**), and the bubble wall thickness (S-R) normalized by the bubble shell (bubble+bubble wall) radius, S (**c**). The effect of yield stress decreases with decreasing bubble wall thickness, and thus, with increasing gas volume fraction.

$$\frac{1}{r^2}\frac{\partial}{\partial r}(r^2 u_r) = 0, \tag{9}$$

where u_r is the bubble growth rate and r is the radial coordinate. Integrating Equation (9) using an instantaneous bubble radius, R, and bubble growth rate, dR/dt, gives

$$u = \frac{R^2}{r^2}\frac{dR}{dt}. \tag{10}$$

Neglecting inertial forces under magmatic conditions, the radial component of the equation of motion for the growth of a spherical shaped bubble is given by

$$\frac{\partial P}{\partial r} = \frac{\partial \tau_{rr}}{\partial r} + 3\frac{\tau_{rr}}{r}. \tag{11}$$

Here $\partial P/\partial r$ is the pressure gradient. τ_{rr} $(= -2\eta\ \partial u_r/\partial r)$ is the radial component of the stress tensor, where η is the dynamic viscosity. From force balance,

$$P_g - P_R + \tau_{rr} = \frac{2\sigma}{R}, \tag{12}$$

where P_R is the melt pressure at the bubble surface. Using Equations (10)-(12), the bubble growth rate in a Newtonian liquid is given by

$$\frac{dR}{dt} = \frac{R}{4\eta}(P_g - P_m - P_\sigma). \tag{13}$$

Here P_g and P_m are the pressure of gas inside the bubble and the pressure of the surrounding melt, respectively. $P_\sigma = 2\sigma/R$ is the pressure due to surface tension forces, where σ is the surface tension.

3.2.2. Pressure loss due to yield stress

The pressure balance during the growth of a spherical bubble of radius R in a yield stress fluid is given by

$$\Delta P = P_g - P_m - P_\sigma - P_y, \tag{14}$$

where ΔP and P_y are the bubble overpressure and the pressure due to yield stress, respectively. The pressure reduction, P_y, during bubble growth due to the presence of yield stress (τ_y) is expressed as (e.g., Yang and Yeh, 1966)

$$P_y = 3.464\tau_y\left[\frac{1}{3} + \ln\left(\frac{S}{R}\right)\right], \tag{15}$$

where S is the summation of bubble radius and bubble wall thickness, and τ_y can be estimated using Equation (8).

Fig. 3b shows that the pressure loss due to yield stress, P_y, decreases with increasing gas fraction, ϕ, at a given normalized crystal fraction, ϕ_x/ϕ_m. The gas volume fraction, ϕ, is calculated from the bubble radius, R, and the half distance between two adjacent bubbles, S, as R^3/S^3. Due to the increase in τ_y, P_y overall increases with increasing ϕ_x/ϕ_m. An increase in bubble radius, R, increases the gas fraction for a given bubble number density. This, in turn, decreases the wall thickness $(S - R)$ surrounding a growing bubble, decreasing the effect of yield stress (Fig. 3c) at a given crystal fraction. Thus, the extent of pressure reduction due to yield stress depends on the competing effects of decompression, crystallization and bubble growth rates in ascending magma during volcanic eruptions.

Table 1
The range of parameter values used in the model.

Model parameters	Description	Parameter values
dP_m/dt (MPa s^{-1})	Magma decompression rate	0.05-5.00
IG^3 (s^{-4})	Rate of crystallization	$10^{-15} - 10^{-5}$
N_b (m^{-3} of melt)	Bubble number density	$10^{13} - 10^{15}$
$P_{initial}$ (MPa)	Initial magma (saturation) pressure	50-100
R_o (m)	Initial bubble radius	$10^{-8} - 10^{-6}$
c_o (wt.%)	Initial water content	2.25-3.25
ϕ_m	Maximum crystal packing fraction	0.30-0.80
n	Flow index	0.20-1.00
τ^*	Yield stress constant	0.20-4.40
η_l (Pa s)	Melt viscosity	10^1-10^6

3.2.3. Effect of yield stress on bubble growth rate

Combining the effects of power-law rheology (e.g., Schwartzberg et al., 1995) and yield stress, the bubble growth rate in crystallizing magma with Herschel-Bulkley rheology can be expressed as

$$\frac{dR}{dt} = \left(\frac{nR^n(P_g - P_m - P_\sigma - P_y)}{4K(2\sqrt{3})^{n-1}}\right)^{\frac{1}{n}}. \tag{16}$$

For $n = 1$ and $\tau_y = 0$ (i.e., $P_y = 0$), the above expression becomes equivalent to the bubble growth in a Newtonian liquid ($K = \eta$; Eq. (13)).

The consistency, K, and flow index, n, are estimated following the formulations in Moitra and Gonnermann (2015) such that

$$K = \eta_l\left(1 - \frac{\phi_x}{\phi_m}\right)^{-2}, \tag{17}$$

and the flow index, n, is defined as

$$n = 1 - (1 - n_{\min})\left(\frac{\phi_x}{\phi_{\max}}\right)^{2.3}. \tag{18}$$

Here $n_{\min}$ and $\phi_{\max}$ are constants at a given modality of crystal size and shape distribution in the magma (Table 1). η_l is the melt viscosity.

Fig. 4 demonstrates that the effect of yield stress becomes significant as $\phi_x \to \phi_m$. With increasing yield stress coefficient (τ^*), the value of yield stress increases according to Equation (8), increasing P_y and decreasing the radius of bubble (R_y) as compared to the bubble radius ($R_{\eta x}$) in the absence of any yield stress, all else being equal. It is assumed

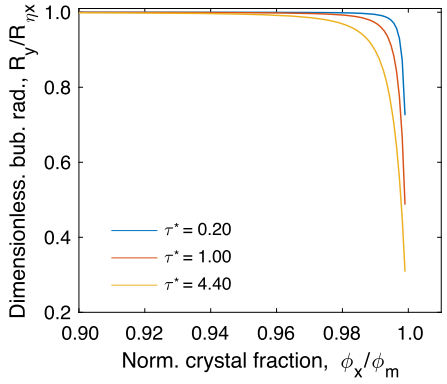

Fig. 4. Dimensionless bubble radius as a function of the normalized crystal faction showing the yield stress-limited growth of bubble (R_y) compared to its growth without the effect of yield stress ($R_{\eta x}$), everything else being equal. τ^* is the yield stress coefficient (Equation (8)). Here the flow index, $n = 1$. This reduction in bubble growth is expected for any magmatic composition due to the significant yield pressure loss (Equation (14)) at high crystal fractions.

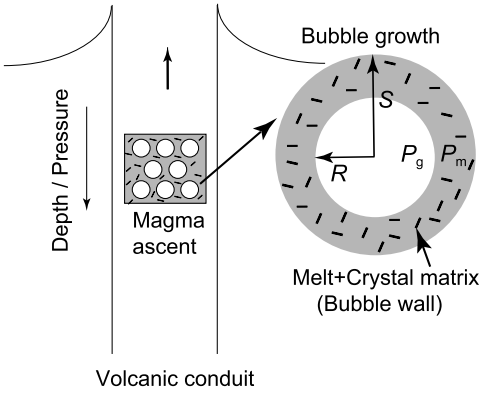

Fig. 5. Schematic diagram (not to scale) shows the conceptual model framework of coupled bubble growth and the ascent of crystallizing magma. The descriptions of the symbols are given under "Notation".

that magma is instantaneously brought to the ambient pressure from an initial pressure of ~100 MPa. For comparison, the shear thinning effect of crystals on magma rheology is not included (i.e., flow index, $n = 1$). Here $R_o = 10^{-8}$ m, $\phi_m = 0.80$ and $N_b = 10^{13}$ m^{-3} of melt. By evaluating for a range of melt viscosity (10-10^6 Pa s), the dimensionless results suggest that this hindrance in bubble growth at high crystal fractions due to yield pressure loss (Equation (14)) is expected for any magmatic composition.

3.3. Modeling bubble growth in ascending and crystallizing magma

To further evaluate the effect of non-Newtonian rheology on bubble growth, I model the mass and momentum balance of decompression and diffusion induced bubble growth coupled with the ascend of crystallizing magma (Fig. 5), assuming that the steady-state magma ascent is adjusted to crystallization and associated rheology. As an example, a typical basaltic melt composition with temperature of 1100 °C (Gamble et al., 1990) is assumed in the model. Because vent exit conditions are expected to be different for volcanic eruptions of given styles, the magma ascent is simplified assuming constant decompression rates, which are varied for a wide range of values suitable for effusive to violently explosive volcanic eruptions. Also, it is assumed that monodisperse spherical bubbles are homogeneously distributed inside a parcel of ascending magma, where melt+crystal matrix is present around the bubbles.

Along with Equation (16), the following conservation equations for bubble and crystal growth are coupled and solved in the model.

$$\frac{d\phi_x}{dt} = 4k_v IG^3 t^3 \exp\left(-k_v IG^3 t^4\right), \tag{19}$$

$$\frac{dc}{dt} = -\frac{4\pi RD(c - c_R)}{V_m} + c\frac{d\phi_x}{dt}\frac{V_{mo}}{V_m}, \tag{20}$$

$$\frac{dP_m}{dt} = -\text{Constant}, \tag{21}$$

$$\frac{dP_g}{dt} = \frac{3BT\rho_m D(c - c_R)}{R^2 M_w} - \frac{3P_g}{R}\frac{dR}{dt}, \tag{22}$$

ϕ_x, c and t are the volume fraction of crystals, the dissolved H_2O content, and the time, respectively. V_{mo} ($= 1/N_b$) is the initial melt volume surrounding one bubble, where N_b is the bubble number density per unit volume of melt. The complete description and units of symbols are listed under 'Notation'.

The crystallization rate is calculated using Equation (19) (e.g., Cashman, 1993), where k_v is the shape factor, I is the nucleation rate and G is the crystal growth rate. For simplicity, IG^3 is assumed to be the crystallization rate that includes the contributions of both the nucleation and growth rates. Equation (20) defines the change in dissolved H_2O concentration in the melt and the diffusion of H_2O inside bubbles. The solubility of H_2O is calculated as a function of pressure, temperature and melt composition following the formulation of Dixon (1997). The basaltic melt viscosity is estimated as a function of the melt composition and the dissolved water content (Hui and Zhang, 2007). The diffusivity of water, D, is calculated following Zhang et al. (2007). The diffusion of H_2O into the bubble is calculated using a mean field approximation (e.g., Toramaru, 1995). The second term on the right-hand side of equation (20) represents the rate of change in dissolved H_2O concentration due to microlite formation and the subsequent reduction in melt volume surrounding the bubble. V_m and V_x are the melt and crystal volumes, respectively. Equation (22) represents the change in gas pressure inside the growing bubbles.

It is assumed that bubbles and crystals are coupled with ascending magma, such that the velocity of all the phases is the same at a given depth within the volcanic conduit (e.g., Mastin, 2002). While the crystallization rate likely increases with increasing decompression rate due to degassing, magma may contain crystals prior to its ascent from crustal chambers, which affect the total crystal content, maximum packing and the rheology of crystalline systems. Accordingly, the crystallization rates are varied for a wide range of values suitable for magma ascent during volcanic eruptions (Shea and Hammer, 2013; Arzilli et al., 2015, 2019) to explore their effects on bubble growth dynamics under a range of magma decompression rates.

The initial magma pressure is calculated from the saturation pressure of the initially dissolved H_2O content. For a wide range of parameter values (Table 1), the models were run until the pressure due to yield stress, P_y, equals the effective bubble overpressure, ΔP_{eff}, which is defined as

$$\Delta P_{\text{eff}} = P_g - P_m - P_\sigma. \tag{23}$$

On the other hand, if P_y stays lower than ΔP_{eff}, models are run until magma reaches the atmospheric pressure. The system of ordinary differential equations (16)-(22) is solved following the approach in Shampine and Reichelt (1997).

3.3.1. Yield stress-limited bubble growth regimes and volcanic eruption styles

The model results exhibit that the extent of crystallization and rheological stiffening primarily depends on the magma decompression and crystallization timescales (Fig. 6). For a relatively high magma decompression rate of ~1 MPa s^{-1}, the crystal volume fraction can be sufficiently high at a greater depth to hinder bubble growth for a relatively high crystallization rate (Regime III). At relatively low crystallization rates, lower values of magma viscosity and yield stress do not significantly hinder bubble growth, and thus, the gas volume fraction continues to increase during magma ascent. This phenomenon is also expected

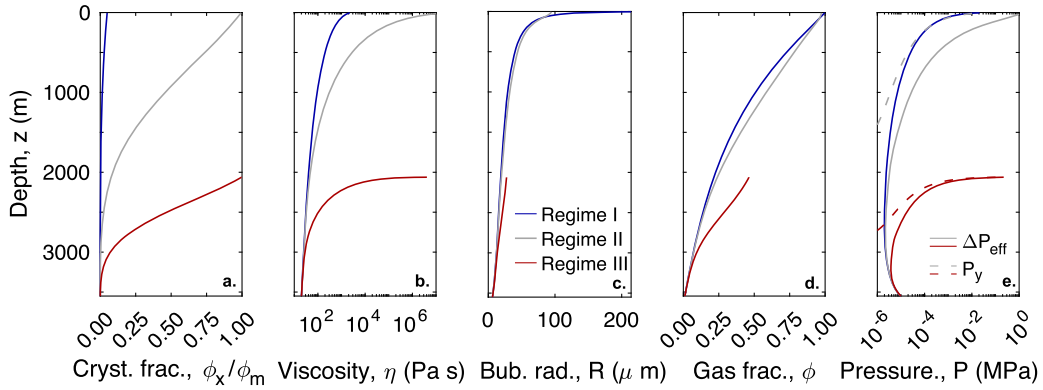

Fig. 6. Typical model results showing the evolution of (**a**) normalized crystal fraction (ϕ_x/ϕ_m), (**b**) magma viscosity (η), (**c**) bubble radius (R), (**d**) gas volume fraction (ϕ), and (**e**) the effective bubble overpressure (ΔP_{eff}) and the pressure reduction due to yield stress (P_y) as functions of depth (z) during magma ascent. Here $R_o = 10^{-8}$ m, $N_b = 10^{13}$ m^{-3} of melt, $\tau^* = 1$, $n = 1$, $\phi_m = 0.80$ and $c_o \sim 3.25$ wt.%. For a given decompression rate (dP_m/dt) of 1 MPa s^{-1}, the crystallization rate (IG^3) is 10^{-10} s^{-4}, $10^{-8.4}$ s^{-4} and 10^{-7} s^{-4} corresponding to regimes I, II and III, respectively (see Fig. 7). Bubbles would stop growing when $P_y = \Delta P_{\text{eff}}$ under regime III (**e**).

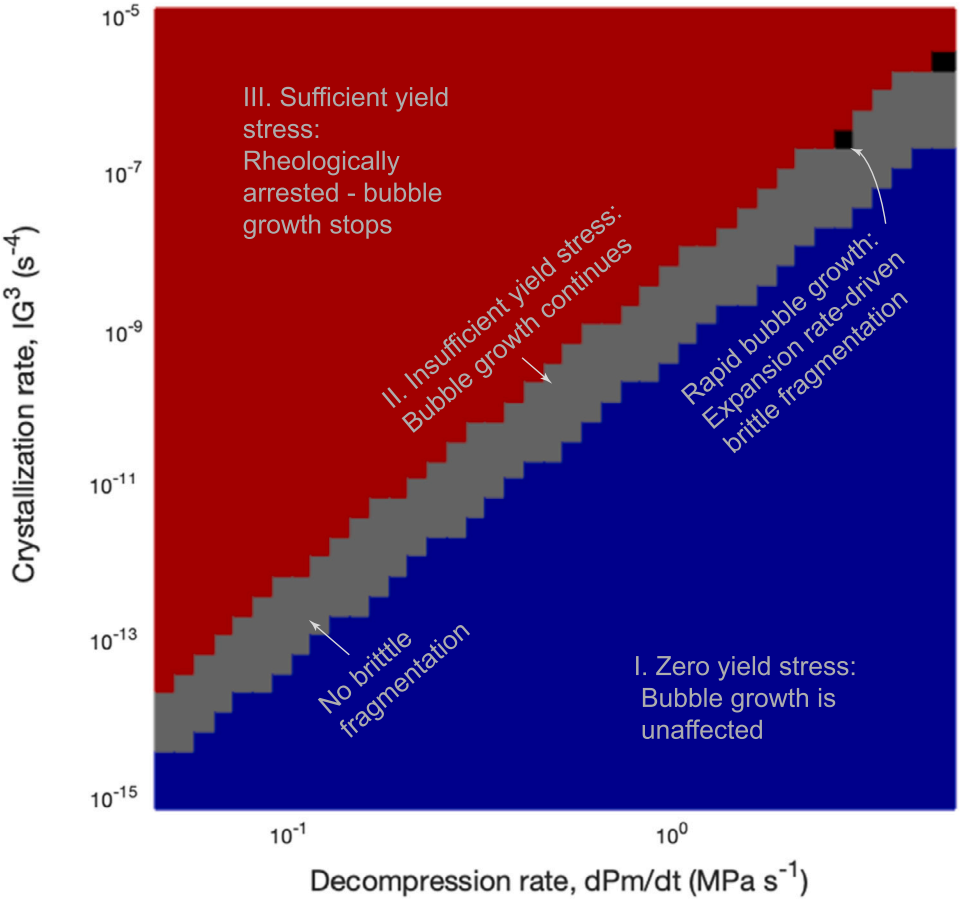

Fig. 7. Bubble growth regimes as functions of magma decompression and crystallization rates: I) The critical crystal fraction required to develop yield stress does not reach ($\phi_x < \phi_c$). II) Yield stress is developed, but larger effective bubble overpressure drives bubble growth ($P_y < \Delta P_{\text{eff}}$; $\phi_x > \phi_c$). III) Yield stress is sufficiently high to stop bubble growth ($P_y \geq \Delta P_{\text{eff}}$; $\phi_x > \phi_c$). Within Regime II, the critical magma expansion rate (~1 s^{-1}) required for brittle fragmentation of crystal-rich ($\phi_x/\phi_m > 0.90$) basaltic magma is reached for a few combinations of parameters (shown in black). Here $R_o = 10^{-8}$ m, $N_b = 10^{13}$ m^{-3} of melt, $\tau^* = 1$, $n = 1$, $\phi_m = 0.80$, and the initial H_2O content, $c_o \sim 3.25$ wt.% corresponds to an initial magma pressure of ~100 MPa.

due to the change in decompression rates at a given crystallization rate, where lower decompression rates overall allow for sufficient crystallization, leading to $P_y \geq \Delta P_{\text{eff}}$.

The model parameter search reveals three distinct regimes of bubble growth in crystallizing magmas (Fig. 7): I) Small crystal fractions ($\phi_x \leq \phi_c$) in the melt cause zero yield stress in bubble walls, and thus bubble growth is only hindered by magma viscosity. II) The crystal content in magma exceeds the threshold fraction ($\phi_x > \phi_c$) generating yield stress, but higher effective bubble overpressure drives bubble growth ($P_y < \Delta P_{\text{eff}}$). III) A sufficient build-up of yield stress causes bubbles to stop growing ($P_y \geq \Delta P_{\text{eff}}$, $\phi_x > \phi_c$). The regimes of bubble growth are less sensitive to bubble number density (N_b), initial bubble radius (R_o) and

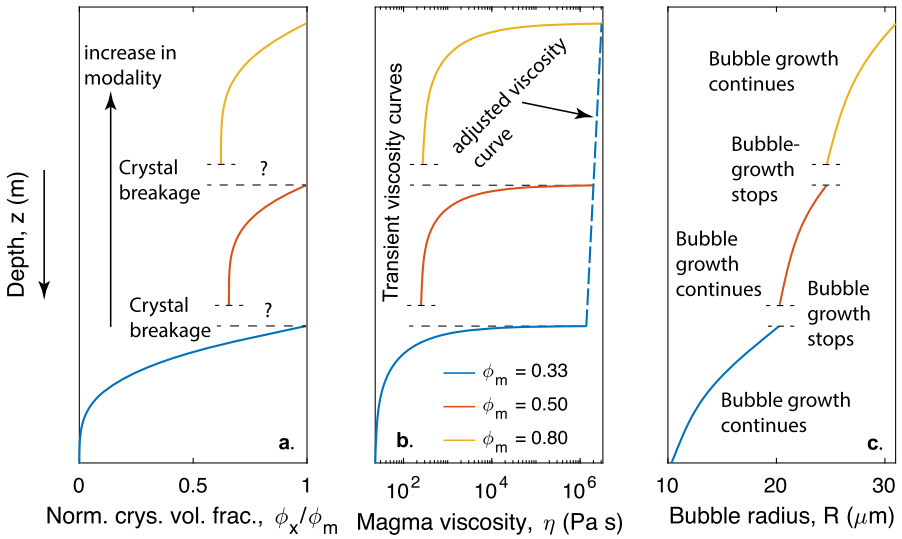

Fig. 8. Periodicity in bubble growth during the ascent of crystal-rich magma. Bubble growth stops as soon as $P_y \geq \Delta P_{\text{eff}}$ as $\phi_x \rightarrow \phi_m$, and it resumes due to crystal breakage and increase in modality until a new maximum packing is adjusted. Here $R_o = 10^{-8}$ m, $N_b = 10^{13}$ m^{-3} of melt, $n = 1$, $\tau^* = 1$, $IG^3 = 10^{-10}$ s^{-4} and $dP_m/dt = 0.1$ MPa s^{-1}. The initial depth is ~3500 m corresponding to a saturation pressure of ~100 MPa. The depth (z) values are kept void as the distance traveled by magma during crystal breakage is unknown.

flow index (n), however, a higher initial water content (c_o) corresponds to a greater saturation pressure, a larger yield stress parameter (τ^*) and a smaller maximum packing fraction (ϕ_m) can increase the normalized crystal content, everything else being equal, broadening the regime of rheological arrest of bubbles (Regime III; see Appendix A).

It is interesting to note that unlike "viscous quench" of bubbles driven by a very high (~10^9 Pa s) viscosity of magma (e.g., Thomas et al., 1994), orders of magnitude smaller viscosity (~10^6 Pa s) of crystal-rich basaltic magma can cause bubbles to stop growing, as the associated yield stress exceeds the effective bubble overpressure (Fig. 6b). Since crystal jamming and development of yield stress are functions of maximum packing, which is a function of crystal shape and modality, this yield stress-driven quenching of bubbles may take place at as low as ~30 volume% of high aspect ratio crystals.

Once bubble growth stops at a high crystal fraction, growth may further resume if the crystal framework is broken or new crystals form changing the modality of the crystalline system. For example, microlites can form in an ascending magma with pre-existing phenocrysts, increasing the maximum packing of the crystalline system (e.g., Cimarelli et al., 2011). On the other hand, crystals might break under shear (Lavallée et al., 2007; Picard et al., 2013), increasing their modality and maximum packing fraction. While the adjusted viscosity of crystalline systems might appear to be increasing with increasing crystal fractions above the maximum packing of the first set of crystals (e.g., Costa et al., 2009), the transient decrease in magma viscosity and yield stress would cause renewed bubble growth until the new crystalline system is adjusted to its maximum packing. Fig. 8 demonstrates that possible crystal breakage and increase in modality may cause a periodicity in bubble growth in magma during volcanic eruptions.

On the other hand, for relatively high crystallization rates (Arzilli et al., 2019) and decompression rates of $\gtrsim 1$ MPa s^{-1} (Moitra et al., 2018) in regime II, the effective overpressure might be sufficient to cause rapid bubble growth at a high crystal content ($\phi_x/\phi_m \gtrsim 0.90$), such that the rate of magma expansion in this regime could reach the critical strain rate of ~1 s^{-1}, required for fragmentation of crystal-rich basaltic magma (Moitra et al., 2018). Although simplified, these results demonstrate that a specific parameter space might be a necessary condition for the Plinian style eruptions of basaltic magma, indicating their relatively infrequent but powerful occurrences in volcanic records.

The styles of volcanic eruptions can further be modified by permeable outgassing (e.g., Eichelberger et al., 1986; Burgisser and Gardner, 2004; Burton et al., 2007; Okumura et al., 2009; Degruyter et al., 2012; Cassidy et al., 2018; Colombier et al., 2017, 2021; La Spina et al., 2021; Bamber et al., 2024), which is not considered in the magma ascent model for simplicity. For high decompression rates correspond to subplinian to Plinian style eruptions, the effect of outgassing is negligible for basaltic and silicic magmas since the decompression time scales are much shorter than the outgassing time scales (e.g., Rust and Cashman, 2011; La Spina et al., 2021; Moitra and Houghton, 2021; Bamber et al., 2022, 2024). For low decompression rates, a decoupling between bubbles and melt with low crystallinity is expected for basaltic magma promoting outgassing (La Spina et al., 2021). The outgassing could also be significant for slowly ascending silicic magmas where bubbles stay coupled with the melt (Degruyter et al., 2012).

If percolation is reached before $\phi_x \rightarrow \phi_m$, efficient loss of pressurized gas would likely decrease the effective bubble overpressure, leading to an effusive eruption. On the other hand, if bubble growth stops before percolation, it will likely not reach during the rest of the magma ascent since the gas fraction may not increase further. For example, Fig. 6d indicates that bubble growth may stop at ϕ <50% which is lower than the typical percolation thresholds for crystallizing basaltic andesitic magmas (Lindoo et al., 2017) and silicic magmas (e.g., Rust and Cashman, 2011). However, since the melt pressure would continue to decrease in the ascending magma, a large build-up of bubble overpressure is expected as magma nears the surface, which may cause eruption explosivity. Furthermore, the segregation of gas between crystal-poor and crystal-rich regions (Pistone et al., 2015; Okumura et al., 2019) can also modify the extent of outgassing. The quantification of bubble growth regimes in this study will likely provide a basis for characterizing such heterogenous processes in future.

4. Conclusion

This study investigates the rheological characteristics of the crystal-rich magma under extensional deformation using dynamically similar analog laboratory experiments. The experimental results show that under extensional deformation, crystal-rich magma exhibits a Herschel-Bulkley type rheology with yield stress and a shear thinning characteristics, similar to the rheology under shear. Using Equation (16) for bubble growth rate in magma with Herschel-Bulkley rheology, it is shown that for any magmatic composition, the presence of yield stress is expected to reduce the bubble overpressure under crystal-rich conditions.

Using a coupled model of bubble growth in an ascending and crystallizing magma, it is further demonstrated that under reasonable eruption conditions, the yield stress could be sufficient to completely halt bubble growth during volcanic eruptions. The model parameter search reveals three distinct regimes of bubble growth: from zero yield stress to yield stress-limited bubble growth to sufficiently high yield stress to stop bubble growth. Although the well-studied crystallization rates for a range of magmatic compositions and eruption styles are used to broadly investigate the effect of yield stress on bubble growth in this study, specific regime boundaries for a given eruption are needed to be evaluated with the conditions specific to that eruption.

One key finding of this study is the sensitivity of the bubble growth regimes to small changes in decompression and/or crystallization rates. The pressure gradient driving magma ascent may change due to the change in magma chamber pressure (e.g., Melnik and Sparks, 1999). Similarly, changes in the crystallization rates due to the variation in the initially dissolved water content (e.g., Hammer, 2008), pre-eruptive storage conditions (e.g., Bamber et al., 2024) or due to a change in the magma decompression rate (e.g., Arzilli et al., 2019) are feasible. The feedback between these variables along with outgassing may further modulate magma fragmentation efficiency, which is required to be investigated in the future. Nonetheless, this study demonstrates that small changes in decompression rates, either independently or in conjunction with small changes in crystallization rates, can cause significant changes in bubble growth dynamics, which may subsequently cause transitions in volcanic eruption styles.

Notation

B	Universal gas constant (8.314 J K^{-1} mol^{-1})
c	Concentration of dissolved volatiles (wt. frac.)
c_R	Concentration of volatiles at the vapor-melt interface (wt. frac.)
D	Diffusivity of H_2O in basalt (m^2 s^{-1})
F	Extensional force (N)
O_F	Objective function (Equation (7))
g	Gravitational acceleration (9.81 m s^{-2})
G	Crystal growth rate (m s^{-1})
I	Crystal nucleation rate (m^{-3} s^{-1})
IG^3	Crystallization rate (s^{-4})
k_v	Volumetric shape factor
K	Consistency (Pa s^n)
L_0	Initial sample length (m)
L_p	Final sample length (m)
M	Torque (N m)
M_w	Molecular weight of water (kg mol^{-1})
n	Flow index
$n_{\min}$	Constant in Equation (18)
N	Number of measured data points
N_b	Bubble number density (m^{-3} per unit volume of melt)
Oh	Ohnesorge number
P	Pressure (Pa)
P_g	Gas pressure inside bubble (Pa)
P_m	Ambient melt pressure outside bubble (Pa)
P_σ	Pressure reduction due to surface tension (Pa)
P_y	Pressure reduction due to yield stress (Pa)
Pe	Peclet number
r	Radial coordinate
r_0	Initial mid-sample radius (m)
r_{mid}	Mid-sample radius (m)
r_p	Plate radius (m)
R	Bubble radius (m)
Re_p	Particle Reynolds number
S	Half distance between two adjacent bubbles (m)
St	Stokes number
t	Time (s)
T	Temperature (°C)
u_r	Bubble growth rate (m s^{-1})
V_m	Volume of melt surrounding one bubble (m^3)
V_{mo}	Initial volume of melt surrounding one bubble (m^3)
V_x	Volume of crystals (m^3)
z	Vertical coordinate
ΔP_{eff}	Effective bubble overpressure (Pa)
η	Bubble wall viscosity (Pa s)
η_E	Extensional viscosity (Pa s)
η_l	Melt viscosity (Pa s)
η_S	Shear viscosity (Pa s)
γ_E	Hencky strain
$\dot{\gamma}$	Strain rate (s^{-1})
$\dot{\gamma}_E$	Extensional rate (s^{-1})
$\dot{\gamma}_S$	Shear rate (s^{-1})
Ω	Angular velocity (rad s^{-1})
ϕ	Gas fraction
ϕ_c	Threshold fraction of crystals (Equation (8))
ϕ_m	Maximum packing fraction of crystals
$\phi_{\max}$	Constant in Equation (18)
ϕ_x	Volume fraction of crystals in the groundmass
ρ_m	Density of magma (kg m^{-3})
σ	Surface tension (N m^{-1})
τ	Stress (Pa)
τ_E	Extensional stress (Pa)
τ_y	Yield stress (Pa)
τ_{rr}	Radial component of stress tensor (Pa)
τ_S	Shear stress (Pa)
τ^*	Constant in Equation (8)

CRediT authorship contribution statement

P. Moitra: Writing – review & editing, Writing – original draft, Methodology, Investigation, Funding acquisition, Conceptualization.

Declaration of competing interest

The authors declare that they have no known competing financial interests or personal relationships that could have appeared to influence the work reported in this paper.

Data availability

The .mat data file generated from the bubble growth modeling and used to plot the growth regimes in Fig. 7 is avaialable at https://doi.org/10.25422/azu.data.26359957

Acknowledgements

The author would like to thank Fabio Arzilli and three anonymous reviewers for their thoughtful comments, and Chiara Maria Petrone for the editorial handling. This research was supported by NSF grant #2202666.

Appendix A. Sensitivity of bubble growth regimes to R_o, τ^*, c_o, N_b, n and ϕ_m

The model parameter search shows that relatively smaller yield stress parameter, τ^* (Fig. A.1), lower initially dissolved water content, c_o (Fig. A.2), and higher maximum packing fraction, ϕ_m (Fig. A.3), everything else being equal, correspond to shallower saturation depth, and shorter decompression and crystallization time scales, reducing the yield pressure, and thus, narrowing Regime III (in red). Changes in the initial bubble radius, R_o (= 10^{-8} m and 10^{-7} m in Fig. 7 and Fig. A.2c, respectively, everything else being equal), bubble number density, N_b, and flow index, n, do not significantly affect the overall results.

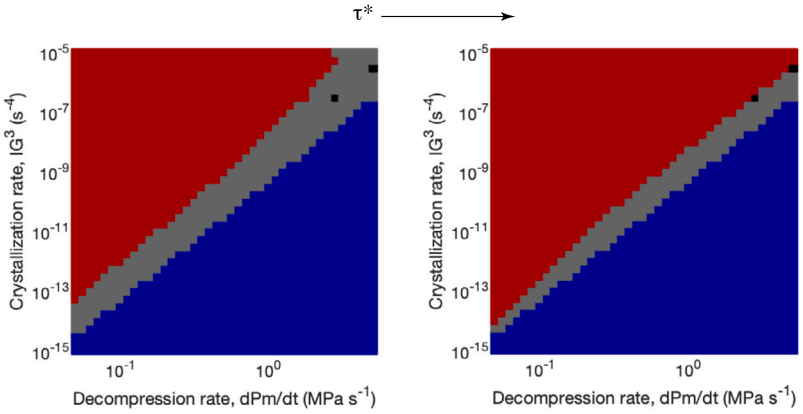

Fig. A.1. Model results show three distinct regimes within crystallization and decompression rates for $R_0 = 10^{-8}$ m, $\phi_m = 0.80$, $n = 1$, $c_o = 3.25$ wt.% and $N_b = 10^{13}$ m^{-3}. The colors in the panels correspond to the regimes in Fig. 7. Red = $P_y \geq \Delta P_{\text{eff}}$; Grey = $P_y < \Delta P_{\text{eff}}$, $\phi_x > \phi_c$; Blue = $\phi_x < \phi_c$; Black = brittle fragmentation of magma. $\tau^* = 0.20$ and 4.40 in (**a**) and (**b**), respectively. The grid resolution is 0.25 and ~0.05 log units for crystallization and decompression rates, respectively, resulting in some undulations at the interfaces of regimes I & II, and II & III (also in Fig. 7 with $\tau^* = 1.0$).

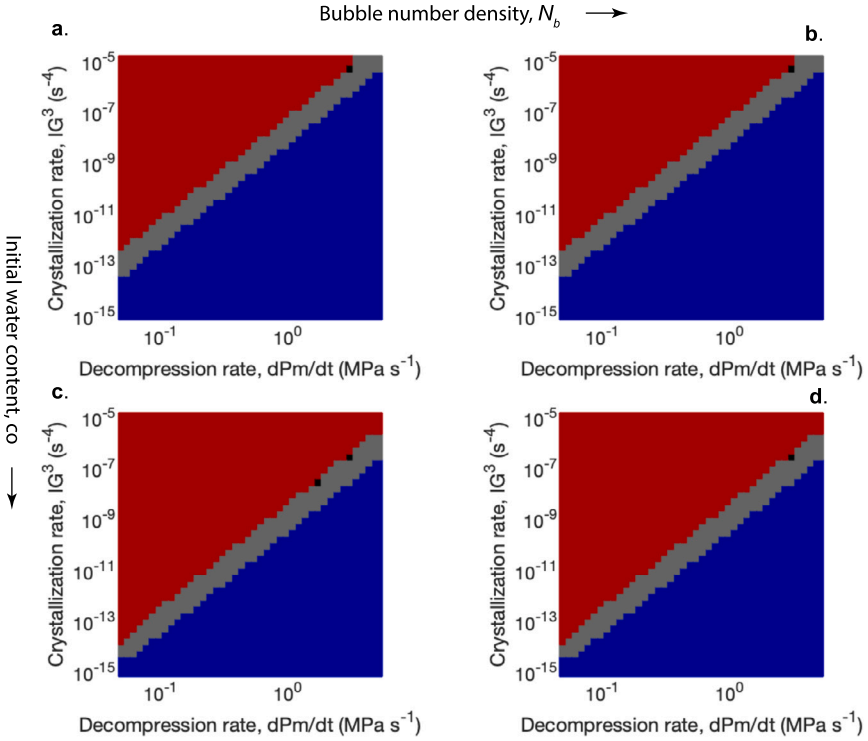

Fig. A.2. Model results show three distinct regimes within crystallization and decompression rates for $R_0 = 10^{-7}$ m, $\phi_m = 0.80$ and $\tau^* = 1$. (**a**) $N_b = 10^{13}$ m^{-3} and $c_o = 2.25$ wt.%, (**b**) $N_b = 10^{15}$ m^{-3} and $c_o = 2.25$ wt.%, (**c**) $N_b = 10^{13}$ m^{-3} and $c_o = 3.25$ wt.%, (**d**) $N_b = 10^{15}$ m^{-3} $c_o = 3.25$ wt.%.

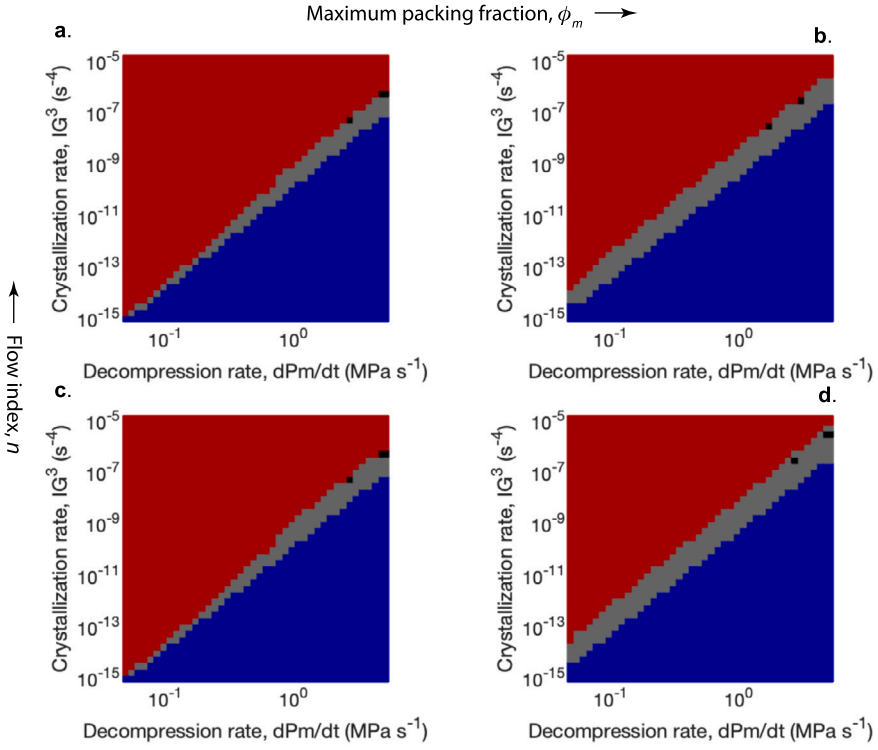

Fig. A.3. The effects of maximum packing fraction, ϕ_m, and flow index, n (shear thinning rheology), on bubble growth regimes. $R_0 = 10^{-7}$ m, $c_o = 3.25$ wt.%, $\tau^* = 1$ and $N_b = 10^{13}$ m^{-3}. (**a**) $n = 1$ and $\phi_m = 0.33$, (**b**) $n = 1$ and $\phi_m = 0.80$, (**c**) n down to ~0.20 as $\phi \rightarrow \phi_m$ and $\phi_m = 0.33$, (**d**) n down to ~0.20 as $\phi \rightarrow \phi_m$ and $\phi_m = 0.80$.

Appendix B. Supplementary material

Supplementary material related to this article can be found online at https://doi.org/10.1016/j.epsl.2024.118984.

References

Andrews, B.J., Befus, K.S., 2020. Supersaturation nucleation and growth of plagioclase: a numerical model of decompression-induced crystallization. Contrib. Mineral. Petrol. 175, 1–20.

Arzilli, F., Agostini, C., Landi, P., Fortunati, A., Mancini, L., Carroll, M., 2015. Plagioclase nucleation and growth kinetics in a hydrous basaltic melt by decompression experiments. Contrib. Mineral. Petrol. 170, 55.

Arzilli, F., La Spina, G., Burton, M.R., Polacci, M., Le Gall, N., Hartley, M.E., Di Genova, D., Cai, B., Vo, N.T., Bamber, E.C., et al., 2019. Magma fragmentation in highly explosive basaltic eruptions induced by rapid crystallization. Nat. Geosci. 12, 1023–1028.

Avard, G., Whittington, A.G., 2012. Rheology of arc dacite lavas: experimental determination at low strain rates. Bull. Volcanol. 74, 1039–1056.

Bamber, E.C., La Spina, G., Arzilli, F., Polacci, M., Mancini, L., de'Michieli Vitturi, M., Andronico, D., Corsaro, R.A., Burton, M.R., 2024. Outgassing behaviour during highly explosive basaltic eruptions. Commun. Earth Environ. 5, 3.

Bamber, E.C., La Spina, G., Arzilli, F., de'Michieli Vitturi, M., Polacci, M., Hartley, M.E., Petrelli, M., Fellowes, J., Burton, M., 2022. Basaltic plinian eruptions at las sierras-masaya volcano driven by cool storage of crystal-rich magmas. Commun. Earth Environ. 3, 253.

Barnes, H.a., 1999. The yield stress — a review or 'panta roi' — everything flows? J. Non-Newton. Fluid Mech. 81, 133–178.

Bergantz, G.W., Schleicher, J.M., Burgisser, A., 2017. On the kinematics and dynamics of crystal-rich systems. J. Geophys. Res., Solid Earth 122, 6131–6159.

Bird, R.B., Stewart, W.E., Lightfoot, E.N., Klingenberg, D.J., 2015. Introductory Transport Phenomena. Wiley Global Education.

Burgisser, A., Gardner, J.E., 2004. Experimental constraints on degassing and permeability in volcanic conduit flow. Bull. Volcanol. 67, 42–56.

Burton, M., Allard, P., Muré, F., La Spina, A., 2007. Magmatic gas composition reveals the source depth of slug-driven strombolian explosive activity. Science 317, 227–230.

Caricchi, L., Burlini, L., Ulmer, P., Gerya, T., Vassalli, M., Papale, P., 2007. Non-Newtonian rheology of crystal-bearing magmas and implications for magma ascent dynamics. Earth Planet. Sci. Lett. 264, 402–419.

Cashman, K.V., 1993. Relationship between plagioclase crystallization and cooling rate in basaltic melts. Contrib. Mineral. Petrol. 113, 126–142.

Cassidy, M., Manga, M., Cashman, K., Bachmann, O., 2018. Controls on explosive-effusive volcanic eruption styles. Nat. Commun. 9, 2839.

Cimarelli, C., Costa, a., Mueller, S., Mader, H.M., 2011. Rheology of magmas with bimodal crystal size and shape distributions: insights from analog experiments. Geochem. Geophys. Geosyst. 12, 1–14.

Colombier, M., Vasseur, J., Houghton, B.F., Cáceres, F., Scheu, B., Kueppers, U., Thivet, S., Gurioli, L., Montanaro, C., Soldati, A., et al., 2021. Degassing and gas percolation in basaltic magmas. Earth Planet. Sci. Lett. 573, 117134.

Colombier, M., Wadsworth, F.B., Gurioli, L., Scheu, B., Kueppers, U., Di Muro, A., Dingwell, D.B., 2017. The evolution of pore connectivity in volcanic rocks. Earth Planet. Sci. Lett. 462, 99–109.

Costa, A., Caricchi, L., Bagdassarov, N., 2009. A model for the rheology of particle-bearing suspensions and partially Molten rocks. Geochem. Geophys. Geosyst. 10, 1–13.

Dai, S., Tanner, R.I., 2017. Elongational flows of some non-colloidal suspensions. Rheol. Acta 56, 63–71.

Degruyter, W., Bachmann, O., Burgisser, a., Manga, M., 2012. The effects of outgassing on the transition between effusive and explosive silicic eruptions. Earth Planet. Sci. Lett. 349–350, 161–170.

Dixon, J.E., 1997. Degassing of alkalic basalts. Am. Mineral. 82, 368–378.

Eichelberger, J., Carrigan, C., Westrich, H., Price, R., 1986. Non-explosive silicic volcanism. Nature, 598–602.

Faroughi, S.A., Huber, C., 2015. A generalized equation for rheology of emulsions and suspensions of deformable particles subjected to simple shear at low Reynolds number. Rheol. Acta 54, 85–108.

Gamble, J.A., Smith, I.E., Graham, I.J., Kokelaar, B.P., Cole, J.W., Houghton, B.F., Wilson, C.J., 1990. The petrology, phase relations and tectonic setting of basalts from the taupo volcanic zone, New Zealand and the Kermadec Island arc-havre trough, SW Pacific. J. Volcanol. Geotherm. Res. 43, 253–270.

Gardner, J.E., Wadsworth, F.B., Carley, T.L., Llewellin, E.W., Kusumaatmaja, H., Sahagian, D., 2023. Bubble formation in magma. Annu. Rev. Earth Planet. Sci. 51, 131–154.

Gonnermann, H.M., Manga, M., 2007. The fluid mechanics inside a volcano. Annu. Rev. Fluid Mech. 39, 321–356.

Gurioli, L., Colo', L., Bollasina, A., Harris, A.J., Whittington, A., Ripepe, M., 2014. Dynamics of strombolian explosions: inferences from field and laboratory studies of erupted bombs from Stromboli volcano. J. Geophys. Res., Solid Earth 119, 319–345.

Hammer, J.E., 2008. Experimental studies of the kinetics and energetics of magma crystallization. Rev. Mineral. Geochem. 69, 9–59.

Hammer, J.E., Cashman, K.V., Hoblitt, R., Newman, S., 1999. Degassing and microlite crystallization during pre-climactic events of the 1991 eruption of mt. pinatubo, Philippines. Bull. Volcanol. 60, 355–380.

Herschel, W.H., Bulkley, R., 1926. Konsistenzmessungen von Gummi-Benzollösungen. Kolloid-Z. 39, 291–300.

Hoover, S.R., Cashman, K.V., Manga, M., 2001. The yield strength of subliquidus basalts - experimental results. J. Volcanol. Geotherm. Res. 107, 1–18.
Hui, H., Zhang, Y., 2007. Toward a general viscosity equation for natural anhydrous and hydrous silicate melts. Geochim. Cosmochim. Acta 71, 403–416.
Ichihara, M., 2008. Dynamics of a spherical viscoelastic shell: implications to a criterion for fragmentation/expansion of bubbly magma. Earth Planet. Sci. Lett. 265, 18–32.
Jones, T., Reynolds, C., Boothroyd, S., 2019. Fluid dynamic induced break-up during volcanic eruptions. Nat. Commun. 10, 3828.
Kolzenburg, S., Chevrel, M.O., Dingwell, D.B., 2022. Magma/suspension rheology. Rev. Mineral. Geochem. 87, 639–720.
La Spina, G., Arzilli, F., Llewellin, E.W., Burton, M.R., Clarke, A.B., de' Michieli Vitturi, M., Polacci, M., Hartley, M.E., Di Genova, D., Mader, H.M., 2021. Explosivity of basaltic lava fountains is controlled by magma rheology, ascent rate and outgassing. Earth Planet. Sci. Lett. 553, 116658.
Lavallée, Y., Hess, K.U., Cordonnier, B., Dingwell, D.B., 2007. Non-Newtonian rheological law for highly crystalline dome lavas. Geology 35, 843–846.
Lensky, N., Navon, O., Lyakhovsky, V., 2004. Bubble growth during decompression of magma: experimental and theoretical investigation. J. Volcanol. Geotherm. Res. 129, 7–22.
Lev, E., Spiegelman, M., Wysocki, R.J., Karson, J.A., 2012. Investigating lava flow rheology using video analysis and numerical flow models. J. Volcanol. Geotherm. Res. 247, 62–73.
Lindoo, A., Larsen, J., Cashman, K., Oppenheimer, J., 2017. Crystal controls on permeability development and degassing in basaltic andesite magma. Geology 45, 831–834.
Mader, H.M., Llewellin, E.W., Mueller, S.P., 2013. The rheology of two-phase magmas: a review and analysis. J. Volcanol. Geotherm. Res. 257, 135–158.
Mastin, L.G., 2002. Insights into volcanic conduit flow from an open-source numerical model. Geochem. Geophys. Geosyst. 3, 1–18.
McKinley, G.H., Sridhar, T., 2002. Filament-stretching rheometry of complex fluids. Annu. Rev. Fluid Mech. 34, 375–415.
Melnik, O., Sparks, R.S.J., 1999. Nonlinear dynamics of lava dome extrusion. Nature 402, 37–41.
Mezger, T.G., 2006. The Rheology Handbook: for Users of Rotational and Oscillatory Rheometers. Vincentz Network GmbH & Co KG.
Moitra, P., Gonnermann, H., 2015. Effects of crystal shape- and size-modality on magma rheology. Geochem. Geophys. Geosyst., 1–26.
Moitra, P., Gonnermann, H.M., Houghton, B.F., Giachetti, T., 2013. Relating vesicle shapes in pyroclasts to eruption styles. Bull. Volcanol. 75, 1–14.
Moitra, P., Gonnermann, H.M., Houghton, B.F., Tiwary, C.S., 2018. Fragmentation and plinian eruption of crystallizing basaltic magma. Earth Planet. Sci. Lett. 500, 97–104.
Moitra, P., Houghton, B.F., 2021. Porosity-permeability relationships in crystal-rich basalts from plinian eruptions. Bull. Volcanol. 83, 71.
Mueller, S., Llewellin, E.W., Mader, H.M., 2011. The effect of particle shape on suspension viscosity and implications for magmatic flows. Geophys. Res. Lett. 38, 1–5.
Namiki, A., Manga, M., 2008. Transition between fragmentation and permeable outgassing of low viscosity magmas. J. Volcanol. Geotherm. Res. 169, 48–60.
Okumura, S., Kushnir, A.R., Martel, C., Champallier, R., Thibault, Q., Takeuchi, S., 2016. Rheology of crystal-bearing natural magmas: torsional deformation experiments at 800 °C and 100 MPA. J. Volcanol. Geotherm. Res. 328, 237–246.
Okumura, S., Nakamura, M., Takeuchi, S., Tsuchiyama, A., Nakano, T., Uesugi, K., 2009. Magma deformation may induce non-explosive volcanism via degassing through bubble networks. Earth Planet. Sci. Lett. 281, 267–274.
Okumura, S., de Silva, S.L., Nakamura, M., Sasaki, O., 2019. Caldera-forming eruptions of mushy magma modulated by feedbacks between ascent rate, gas retention/loss and bubble/crystal framework interaction. Sci. Rep. 9, 1–12.
Oppenheimer, J., Rust, A.C., Cashman, K.V., Sandnes, B., 2015. Gas migration regimes and outgassing in particle-rich suspensions. Front. Phys. 3, 60.
Papale, P., 1999. Strain-induced magma fragmentation in explosive eruptions. Nature 397, 425–428.
Petrone, C.M., Mollo, S., Gertisser, R., Buret, Y., Scarlato, P., Del Bello, E., Andronico, D., Ellis, B., Pontesilli, A., De Astis, G., et al., 2022. Magma recharge and mush rejuvenation drive paroxysmal activity at Stromboli volcano. Nat. Commun. 13, 7717.
Picard, D., Arbaret, L., Pichavant, M., Champallier, R., Launeau, P., 2013. The rheological transition in plagioclase-bearing magmas. J. Geophys. Res., Solid Earth 118, 1363–1377.
Pinkerton, H., Stevenson, R.J., 1992. Methods of determining the rheological properties of magmas at sub-liquidus temperatures. J. Volcanol. Geotherm. Res. 53, 47–66.
Pistone, M., Arzilli, F., Dobson, K.J., Cordonnier, B., Reusser, E., Ulmer, P., Marone, F., Whittington, A.G., Mancini, L., Fife, J.L., et al., 2015. Gas-driven filter pressing in magmas: insights into in-situ melt segregation from crystal mushes. Geology 43, 699–702.
Proussevitch, A.A., Sahagian, D.L., Anderson, A.T., 1993. Dynamics of diffusive bubble growth in magmas: isothermal case. J. Geophys. Res. 98, 22283.
Rust, a.C., Cashman, K.V., 2011. Permeability controls on expansion and size distributions of pyroclasts. J. Geophys. Res., Solid Earth 116, 1–17.
Ryerson, F.J., Weed, H.C., Piwinskii, a.J., 1988. Rheology of subliquidus magmas: 1. Picritic compositions. J. Geophys. Res. 93, 3421.
Sable, J.E., Houghton, B.F., Del Carlo, P., Coltelli, M., 2006. Changing conditions of magma ascent and fragmentation during the Etna 122 BC basaltic Plinian eruption: evidence from clast microtextures. J. Volcanol. Geotherm. Res. 158, 333–354.
Sable, J.E., Houghton, B.F., Wilson, C.J.N., Carey, R.J., 2009. Eruption Mechanisms During the Climax of the Tarawera 1886 Basaltic Plinian Eruption Inferred from Microtextural Characteristics-of the Deposits. Special Publications of IAVCEI, pp. 129–154.
Schwartzberg, H.G., Wu, J.P., Nussinovitch, A., Mugerwa, J., 1995. Modelling deformation and flow during vapor-induced puffing. J. Food Eng. 25, 329–372.
Shampine, L.F., Reichelt, M.W., 1997. The MATLAB ODE suite. SIAM J. Sci. Comput. 18, 1–22.
Shea, T., Hammer, J.E., 2013. Kinetics of cooling- and decompression-induced crystallization in hydrous mafic-intermediate magmas. J. Volcanol. Geotherm. Res. 260, 127–145.
Soldati, A., Sehlke, A., Chigna, G., Whittington, A., 2016. Field and experimental constraints on the rheology of arc basaltic lavas: the January 2014 eruption of pacaya (Guatemala). Bull. Volcanol. 78, 1–19.
Sparks, R., 1978. The dynamics of bubble formation and growth in magmas: a review and analysis. J. Volcanol. Geotherm. Res. 3, 1–37.
Suckale, J., Keller, T., Cashman, K.V., Persson, P.O., 2016. Flow-to-fracture transition in a volcanic mush plug may govern normal eruptions at Stromboli. Geophys. Res. Lett. 43, 12–071.
Szabo, P., 1997. Transient filament stretching rheometer: I: force balance analysis. Rheol. Acta 36, 277–284.
Thomas, N., Jaupart, C., Vergniolle, S., 1994. On the vesicularity of pumice. J. Geophys. Res., Solid Earth 99, 15633–15644.
Toramaru, A., 1995. Numerical study of nucleation and growth of bubbles in viscous magmas. J. Geophys. Res., Solid Earth 100, 1978–2012. pp. 1913–1931.
Villermaux, E., 2012. The formation of filamentary structures from Molten silicates: Pele's hair, angel hair, and blown clinker. C. R., Méc. 340, 555–564.
Vona, A., Romano, C., Giordano, D., Russell, J.K., 2013. The multiphase rheology of magmas from Monte Nuovo (Campi Flegrei, Italy). Chem. Geol. 346, 213–227.
Walsh, S.D.C., Saar, M.O., 2008. Magma yield stress and permeability: insights from multiphase percolation theory. J. Volcanol. Geotherm. Res. 177, 1011–1019.
White, E.E.B., Chellamuthu, M., Rothstein, J.P., 2010. Extensional rheology of a shear-thickening cornstarch and water suspension. Rheol. Acta 49, 119–129.
Yang, W.J., Yeh, H.C., 1966. Theoretical study of bubble dynamics in purely viscous fluids. AIChE J. 12, 927–931.
Zhang, Y., 1999. A criterion for the fragmentation of bubbly magma based on brittle failure theory. Nature 402, 648–650.
Zhang, Y., Xu, Z., Zhu, M., Wang, H., 2007. Silicate melt properties and volcanic eruptions. Rev. Geophys. 45, 1–27.